NON-LINEAR STATIC AND DYNAMIC ANALYSIS OF ROCKING MASONRY CORNERS USING RIGID MACRO-BLOCK MODELLING

Claudia Casapulla[a*], Linda Giresini[b], Luca Umberto Argiento[a], Alessandra Maione[a]

[a] Department of Structures for Engineering and Architecture, University of Naples Federico II, via Forno Vecchio 36, 80134, Naples, Italy

[b] Department of Energy, Systems, Territory and Constructions Engineering, University of Pisa, Largo Lucio Lazzarino 1, 56100, Pisa, Italy

*Corresponding author (Claudia Casapulla)

Ph/fax: +39 081 2538901

E-mail: casacla@unina.it

ABSTRACT

The corner failure is one of the most typical local mechanisms in masonry buildings vulnerable to earthquakes. The seismic assessment of this mechanism is poorly studied in the literature and in this paper it is addressed by means of both non-linear static and dynamic analyses of rocking rigid blocks. The static approach is based on the displacement-based method and is aimed at predicting the onset of the 3D failure mechanism and its evolution through incremental kinematic analysis. This approach also considers the presence of a thrusting roof and the stabilising contribution of frictional resistances exerted within interlocked walls. The capacity in terms of both forces and displacements is compared with the seismic demand through the construction of acceleration-displacement response spectra, with some originality. The non-linear dynamic approach is based on the seminal Housner's work on rocking rigid blocks and considers the influence of transverse walls, roof overloads and outward thrust, all included in an updated equation of one-sided motion. In particular, the process of defining an equivalent prismatic block, representative of the original corner geometry, is presented to convert the 3D dynamic problem into a 2D rocking motion. The wide suitability and advantage of such modelling approaches to assess the seismic response of rocking masonry structures with reference to specific limit states are demonstrated through a real case study, i.e. the collapse of a

corner in a masonry school building during the 2016-17 Central Italy seismic sequence. The compared results provide a good agreement of predictions in terms of both onset and overturning conditions, for which the static model appears to be more conservative than the dynamic one.

KEYWORDS

Incremental kinematic analysis, dynamics of rigid blocks, out-of-plane behaviour, frictional resistances, horizontal restraint, 2016-17 Central Italy Earthquakes.

1. INTRODUCTION

The "box-type" behaviour of a masonry building generally requires the presence of well-connected walls and floors and a proper horizontal stiffness of the floors. In this case, proper modelling procedures can be adopted to simulate the in-plane effects of seismic actions on buildings, possibly experimentally evaluating the masonry mechanical properties [1]. All modern codes for seismic design of new masonry buildings usually provide dimensioning and detailing regulatory requirements that make out-of-plane failure almost improbable to occur even under severe seismic load.

Conversely, in masonry buildings without a box-type behaviour, such as most existing masonry buildings in the historic city centres, local out-of-plane failures can take place, especially of peripheral walls and even under low intensities of ground motion [2]. In fact, the main deficiencies in such buildings are the lack of proper connections between orthogonal walls, the absence of connecting ties, insufficiently rigid floor diaphragms, low strength and deterioration of materials; the presence of openings and their position in the walls are further relevant aspects. In addition, the low strength/mass ratio of such structures increases their vulnerability in out-of-plane direction since inertia forces are not restrained because of reduced stiffness and strength of the masonry walls in that direction.

It has been recognized, in particular, that the most recurrent failure modes caused by seismic forces acting orthogonally to the building walls involve overturning mechanisms, which can be represented by simple or complex rocking of parts of masonry walls. In case of simple rocking, poor wall-to-wall and wall-to-horizontal structure connections and/or flexible horizontal structures cause the separation of orthogonal walls and the single walls start to rock separately under seismic excitations (Figure 1a). The complex rocking, instead, can be caused by similar conditions but with good wall-to-wall connections and it refers to rocking walls together with parts of orthogonal walls (Figure 1b) or rocking corners (Figure 1c). These kinds of local failure generally occur when a monolithic behaviour can be guaranteed for walls so that they can be regarded as rigid blocks.

With this assumption, their out-of-plane seismic response can be treated following two fundamental approaches in static and dynamic fields, i.e. the pioneering Heyman's and Housner's works respectively [3,4].

(a) (b) (c)

Figure 1 Simple (a) and complex (b) rocking of masonry walls; corner failure as complex rocking of masonry walls (c).

However, the assessment of the rocking and overturning response of rigid blocks to earthquakes is still a complex task due to the large variability of the mechanical properties of the materials, the uncertainty about the construction sequence and the high sensitivity of the models to the input motion, variations in geometry and dissipation issues, especially for historical constructions [5–7]. Several methods and tools based on different approaches have lately been attempted to address this complex but valuable topic. In fact, as comprehensively discussed in [8–11], there is a large quantity of literature focused on force-based, displacement-based and rocking approaches. Some addressed aspects are also valuable to evaluate structural and energy retrofitting strategies for masonry walls [12,13].

On the other hand, despite the increasing interest of the scientific community in this topic, there is still a lack of reliable modelling strategies to statically and dynamically simulate all the types of local mechanisms and to include the significant contributions of possible restraints of the failing parts of masonry [14–16]. In particular, the corner failure involving a complex three-dimensional motion is still poorly investigated. In fact, although this kind of failure has frequently been observed in seismic scenarios, only few analytical works [17–20] and experimental investigation [21] devoted to it were found in the literature. Generally, it can occur when at least one corner of the building is free, without any adjacent structures, i.e. for buildings isolated or positioned at the end of a block. The vulnerability of this mechanism is increased by the destabilizing contribution of the roof (Figure 1c) and the presence of openings near the edge.

79 To fill this gap of the literature, this paper is particularly focused on the modelling of rocking masonry corners by means of
80 two approaches in comparison: the non-linear static and dynamic models, based on the limit analysis method and the
81 Housner's theories of rocking rigid blocks, respectively. The two models of the rocking masonry corners are extensively
82 discussed in their assumptions, theoretical background and field of application, with particular focuses on their novel aspects
83 with respect to the previous works on this failure mechanism. The potential of the two approaches in defining the onset and
84 overturning conditions of any rigid block and in evaluating its seismic safety will be shown for a particular case study: the
85 collapse of a corner in a masonry school building during the 2016-17 Central Italy seismic swarm.
86 As far as the non-linear static analysis is concerned, the modelling approach is based on the displacement-based method aimed
87 at predicting both the onset failure mechanism of the rocking rigid block and the evolution of its motion in large displacements.
88 The solution procedure follows the incremental kinematic analysis proposed by Lagomarsino [22], which is herein developed
89 to include the contribution of frictional resistances and a thrusting roof. The onset of the symmetric and non-symmetric corner
90 failure has already been described in [19,21], through the minimization of the load factor. Instead, the evolution of the motion
91 in large displacements is originally developed in this paper in order to construct pushover curves, capacity curves of the
92 equivalent non-linear Single Degree Of Freedom system (SDOF) and capacity thresholds representing defined limit states.
93 When the model is applied to the real case study, its capacity in terms of both forces and displacements is compared with the
94 seismic demand through the construction of Acceleration-Displacement Response Spectra (ADRS) [23]. To this aim, another
95 novel aspect of the model is presented: its capability of treating the 3D problem as 2D problems by considering the
96 superimposition of these curves along the planes of the two interlocked walls. This strategy is also necessary to meet the
97 availability of the recorded seismic inputs in these two directions.
98 As regards to the non-linear dynamic analysis of rigid blocks, which started with the pioneering Housner's work, the masonry
99 walls are assumed as rigid; their motion takes into account dissipation of energy over each impact. The model is extremely
100 intuitive, and, although bouncing and sliding are neglected, it was demonstrated to be quite reliable to reproduce the real
101 behaviour of monolithic masonry walls [14,24]. Similarly to non-linear static analysis, also rocking analysis can be applied
102 to a masonry element, both in free condition (namely, without added restraints such as tie-rods) and in a configuration where
103 horizontal restraints, such as transverse walls and steel tie-rods, are active during motion, both in one-sided and two-sided
104 conditions [25,26]. In particular, the three-dimensional motion of the rocking masonry corner, in principle complex to treat,
105 is originally simplified into a two-dimensional problem, where a prismatic equivalent block is associated to the corner
106 mechanism.

In sum, the novel contributions of this paper can be recognized not only in the investigation of the corner failure in masonry buildings, which is still poorly studied in the literature, but also in the great suitability of each of the two proposed approaches to represent the 3D motion of the complex out-of-plane mechanism and in the interesting comparison of their results.

The paper is organized as follows. Sections 2 and 3 contain the fundamentals of the non-linear static and non-linear dynamic analysis in theoretical and analytical terms, discussing the procedures to apply them to the case of the corner failure in masonry buildings. Section 4 presents the application of the analysis methods to a real case study, i.e. the collapse of a corner in a masonry school building during the 2016-17 Central Italy seismic sequence. The results of the two presented approaches are compared and discussed in Section 0 with reference to specific limit states and with a particular insight in the actual onset and the near-collapse conditions. Some conclusions are drawn in Section 6.

2. NON-LINEAR STATIC ANALYSIS OF ROCKING CORNERS

According to the kinematic approach of the equilibrium limit analysis, local mechanisms in masonry buildings can be considered as kinematic chains of masonry portions, regarded as rigid macro or micro-block assemblages, interacting through interface elements [3]. Horizontal static actions, expressed as a percentage of the dead loads by means of a load factor, are applied to the centre of mass of each moving element, in addition to all the other external loadings. The horizontal acceleration causing the mechanism is defined depending on the load factor. Therefore, in formulating all the feasible mechanisms, the lowest value of the load factors expressing limit equilibrium configurations corresponds to the onset of the most likely failure mode and to the maximum capacity of the wall to resist earthquakes.

According to the displacement-based method, pushover curves can then be obtained from the static load factors (non-linear static analysis). These are obtained by the application of the theorem of virtual works, considering varied kinematic configurations of the examined mechanism, in large displacements. Along this incremental kinematic analysis, the contribution of links is taken into account, till the ultimate equilibrium condition [22,27].

Despite its simplicity, this approach becomes rather complicated when frictional resistances are taken into account, as generally occurs in actual failures [17]. In fact, proper assumptions need to be made on the flow rules to define associative or non-associative solutions when using limit analysis [28]. These assumptions involve important implications on the value of collapse load multiplier and the failure mechanism, considering that, generally speaking, non-associated flow rules do not guarantee unique solutions to the limit analysis problems (non-standard limit analysis) [29]. In addition, for complex mechanisms, interactions among rocking, sliding and twisting of connected rigid macro or micro-blocks should be taken into

account to define the most likely in-plane or out-of-plane failure mechanisms, at the onset and during the evolution of the kinematic chain [30].

An advanced macro-block modelling approach including frictional resistances [19,31] has demonstrated to be capable of approaching the "exact" solutions for both in-plane and out-of-plane onset of mechanisms, with better results in comparison with other macro and micro-block models, also with the great advantage of obtaining such solutions with a considerably lower computational effort than the micro-block modelling approaches. This model is also suitable to perform pushover analyses using incremental kinematics, as shown in [15] for simple rocking walls weakly connected with sidewalls and in this paper for the complex rocking corner.

Therefore, it can be applied to any kind of local failure mechanism in masonry buildings, provided that the external and internal loadings are clearly defined. In the following, an accurate evaluation of the frictional resistances and the definition of reliable collapse load factors are developed. The pushover curves and the ADRS superimposed to the capacity curves will be presented in Section 4 with reference to the selected real case study.

2.1. Rigid macro-block model

The adopted macro-block model is based on the assumptions for the constituent micro-blocks (or units) of infinite strength in compression, tension and shear and no-tension and frictional behaviour at their contact interfaces (Coulomb failure criterion) [27]. Masonry block walls with regular units and staggering are concerned (single-leaf walls arranged in a running bond pattern), the cracking and crushing of micro-blocks are ignored and the plastic dissipation due to friction is reduced to contact interfaces. The cracks are considered as average inclinations of the discontinuous lines following the disposition of joints which tends to separate the walls in macro-blocks. The crack pattern of the mechanism is represented by the inclination of the crack lines, which are not assigned a priori but are variables of the problem, depending on geometrical and mechanical parameters.

With reference to the corner failure in a masonry building, which generally involves well-connected masonry walls under orthogonal forces, the possible mechanism can be simplified as a combination of two failure modes: the rocking-sliding failure, with the formation of two main cracks that break the continuity of the interlocked walls [19], and the horizontal flexure failure, with the formation of two macro-blocks rotating around three cylindrical hinges [21]. The geometrical parameters, mainly the unit shape, strongly affect the prevalence of one over the other and in this paper only the rocking-sliding failure is considered, while neglecting the flexural effects. This is the case of walls composed of rather square blocks, as those belonging to the real case study analyzed in Sections 4 and 5. This failure mode is characterized by a prismatic wedge rotating around a

hinge placed at its vertex, involving rocking-sliding motions along the crack lines. Mostly, the corner failure involves the top level of a masonry building for the whole floor height since it is mainly activated in the presence of roofs inclined in both directions and openings very close to the edges.

Figure 2a presents a recurrent geometry of the corner failure with the presence of openings within the interlocked walls. These are denoted Wall 1 and Wall 2, respectively oriented along the Cartesian Y and X axes, and are assumed to have the same thickness s, for the sake of simplicity. The wedge, identified by the main cracks, is highlighted in pink colour and the overloads of a hipped roof are assumed to be transferred by a hip rafter to the intersection of the walls, disposed along the bisector plane of the corner, as commonly occurs. The overloads are the inertial forces and the static thrust T_s inclined of 45° with respect to X and Y axes. Point G is the centre of all the involved masses, e.g. the mass of the rocking macro-block plus the masses of the roof.

Due to non-symmetric conditions in geometry and loading of the 3D failure mechanism, the vertical plane of rotation does not coincide with the corner bisector plane. In fact, the inclination γ of its trace OG on the horizontal XY-plane with respect to YZ-plane is dependent on the geometry of the unknown crack pattern (Figure 2b) and therefore on the coordinates of point G. On the other hand, it is easy to recognize that the direction of the horizontal forces and the frictional resistances is parallel to the line joining OG and the rotation axis ω is orthogonal to this line on the horizontal plane.

The internal and external actions displayed on Figure 2 are: F in different positions as the weighted frictional resistances, W as the generic weights and overloads and T_s as the horizontal thrust transferred by the hip rafter. In particular, F are evaluated by applying the criterion proposed and updated in previous works [19,31]. This criterion concerns the formulation of the frictional resistances in function of the variable inclinations of the crack lines, based on the occurrence that these resistances tend to their maximum values as the crack lines tend to the vertical direction, while approaching zero as the crack lines tend to their maximum values, i.e. the half-unit shape line. The latter is defined as the angle $\alpha_b = \tan^{-1}(v/h_b)$, where $v = l_b/2$ is the overlapping length between two units (Figure 2c).

According to this criterion, the resultant frictional resistances activated along the inclined crack lines of the rocking corner strictly depend on the inclination angles and should also account for the contribution due to the overloading in addition to the own weight of the interlocked walls. In fact, the upper bound of the actual frictional resistance for each wall is given by the maximum resultant of these two contributions, i.e.:

$$F_{\max} = F_W + F_Q \tag{1}$$

where:

$$F_W = \sum_{1}^{n} S_i = W_b \frac{n(n+1)}{2} f; \qquad F_Q = qnvf \tag{2}$$

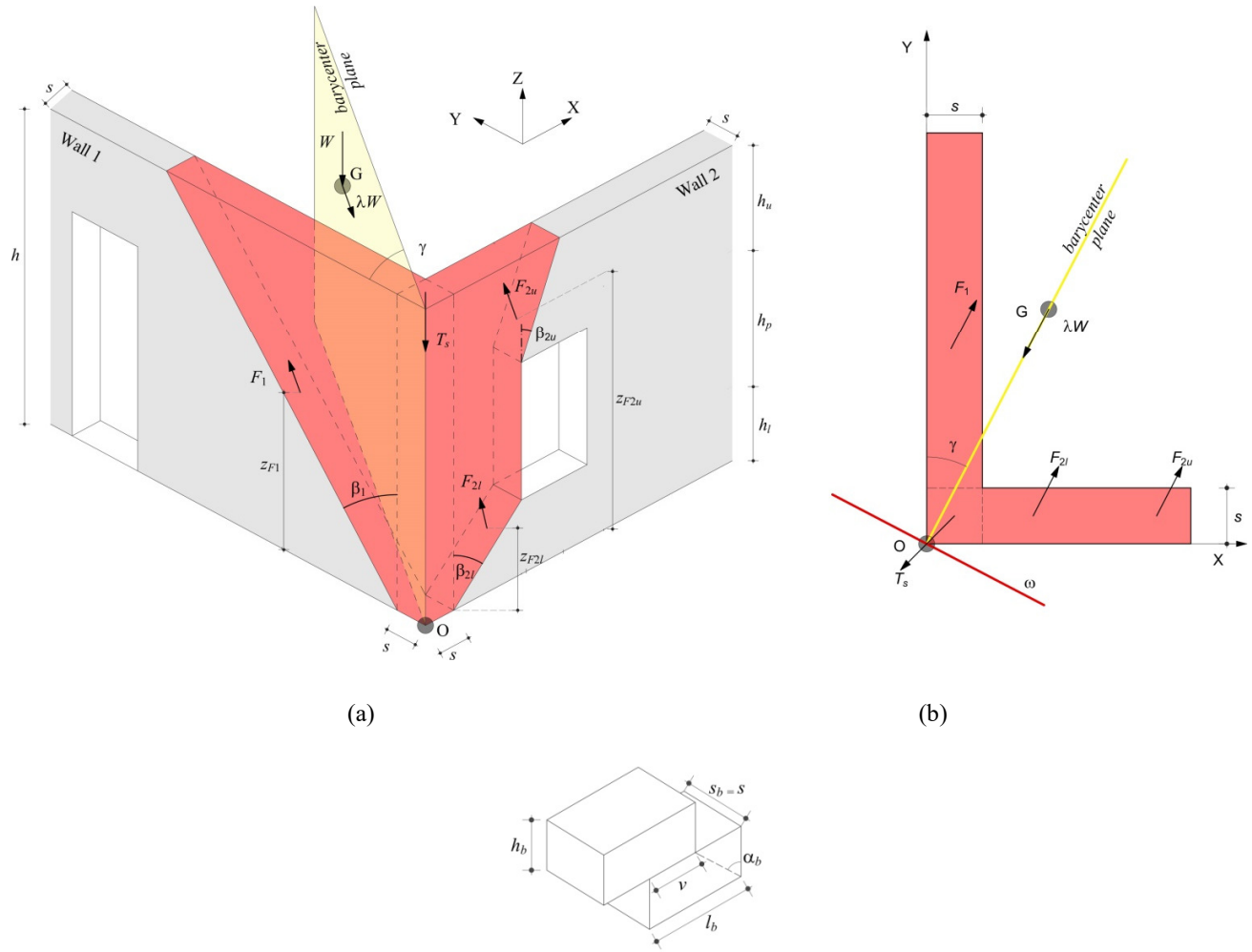

(a) (b)

(c)

Figure 2 Corner failure (a), projection of the rocking wedge on the horizontal XY-plane (b), masonry unit dimensions (c).

Specifically, S_i is the limiting shear force due to friction at contact interface i, W_b is the weight of a single half-unit, n is the number of rows along the wall height, f is the friction coefficient, while q is the uniformly distributed overload for unit of wall length. The application points of the stabilizing forces F_W and F_Q were found to be at about 2/3 of the height h and half-height from the top of the generic crack line [31], respectively.

The actual resultant of the frictional resistances along each crack line can be evaluated as a weighted value in function of the crack inclination angle, i.e. [19]:

$$F = F_{\max}\left(1 - \frac{\beta}{\alpha_b}\right) \tag{3}$$

where β and α_b are the inclination of the generic crack line and of the half-unit shape, respectively.

2.2. Non-linear kinematic approach

The solution procedure to statically assess the seismic capacity of the examined rocking mechanisms is based on the kinematic approach of limit analysis and is first aimed at identifying the geometry of the moving macro-blocks (not known a priori) which minimizes the onset load factor. A subsequent pushover analysis is made by considering geometric non-linearity, that is, by evaluating the load factor for varied kinematic configurations, as a function of the displacement of a control point.

By considering a varied configuration of the rocking corner represented by a finite rotation ϑ within the rotation plane (Figure 3), the virtual work performed by the resultant of the inertial forces W, applied on its centre of mass G, can be expressed by the relation:

$$L_W = \lambda W z \phi - W x \phi \tag{4}$$

where ϕ is the virtual rotation and xy_W and z_W are the horizontal and vertical distances of the rotated point G from the hinge, respectively. These, together with the angular position ρ_W of the same point, are:

$$xy_W = R_W \cos(\rho_W + \vartheta)\,; \qquad z_W = R_W \sin(\rho_W + \vartheta)\,; \qquad \rho_W = \tan^{-1}\left(\frac{h_w}{s_w}\right) \tag{5}$$

where R_W is the radius vector connecting the pivot point O to the actual centre of mass G.

The virtual work performed by the other horizontal forces $F_{1,2l,2u}$ and component of T_s parallel to OG can be expressed in a similar way by only considering their vertical distances from the hinge (Figure 2). Thus, the load factor is simply derived from the application of the Virtual Work Principle as:

$$\lambda = \frac{W x y_W + F_1 z_{F1} + F_{2l} z_{F2l} + F_{2u} z_{F2u} - \frac{\sqrt{2}}{2} T_s (a_1 + a_2) z_T}{W z_W} \tag{6}$$

where $a_1 = \sin\gamma$, $a_2 = \cos\gamma$ (Figure 2). It is easy to verify that λ corresponds to the onset load factor for $\vartheta = 0$ (Figure 3a).

The assumed 3D configuration of the mechanism is defined by two unknown angles of crack (Figure 2a):

1) the inclination of the crack line with respect to the vertical Z-axis, say $\tan\beta_1$, for Wall 1 along Y-axis;

2) the inclination of the upper crack line above the opening within the spandrel, represented by $\tan\beta_{2u}$, for Wall 2 along X-axis.

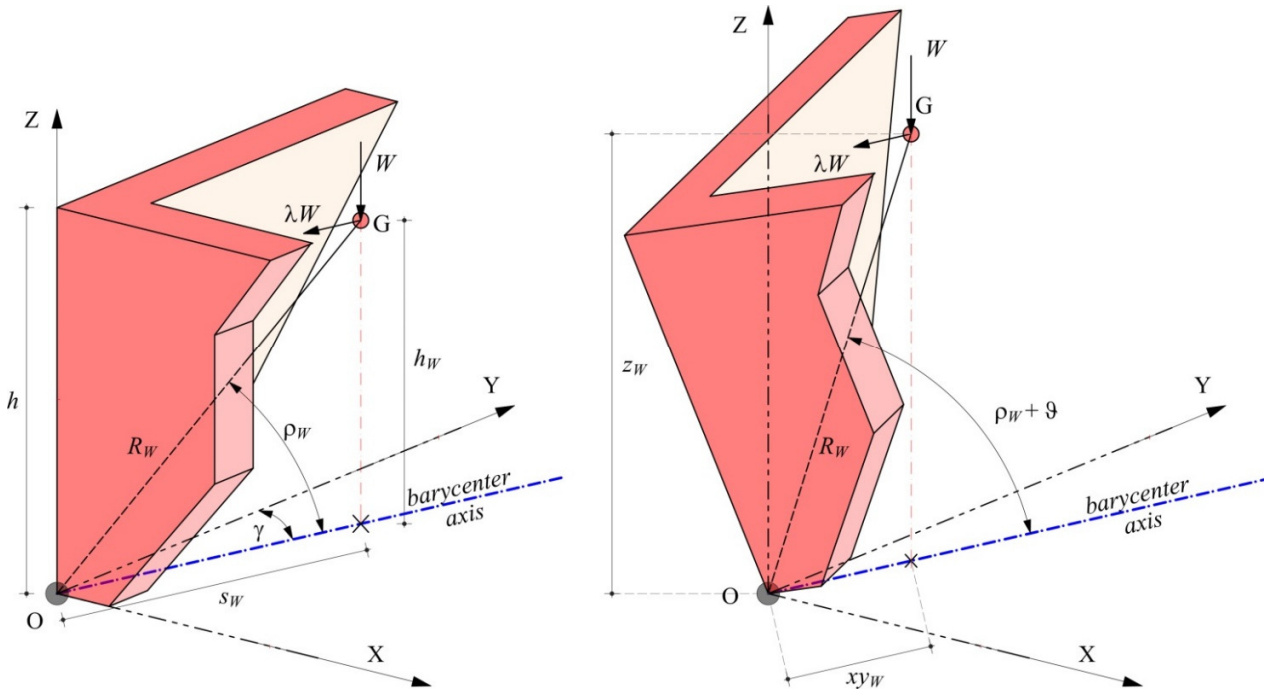

(a) (b)

Figure 3 Initial (a) and varied (b) kinematic configurations of the corner.

The two unknown variables $\tan\beta_1$ and $\tan\beta_{2u}$ that define the most likely failure configuration of the rocking corner are hence calculated through the condition of minimization of λ, under the following geometrical constrains:

$$0 \leq \tan\beta_1 \leq \tan\beta_{1\max}; \qquad 0 \leq \tan\beta_{2u} \leq \tan\beta_{2u\max} \qquad \text{with: } \tan\beta_{1\max} = \tan\beta_{2u\max} = \tan\alpha_b \tag{7}$$

Pushover curves can then be performed from the static load factor. These curves are characterized by different phases of motion depending on the active contributions of links, till the ultimate equilibrium condition. A detailed description of the curves and the associated phases can be found in Section 4.2 where the model is applied to the masonry corner of the case study. The evolution of these phases in terms of the load factor and displacement is governed by the same Eq. (6) with updated coordinates of the application points, according to Eq. (5). The control point can be assumed as the same point for all phases, e.g. the centre of mass of the masonry portion only. Its displacement is affected by the variation of xy_W, i.e.:

$$d_{CG} = s_W - xy_W \tag{8}$$

The incremental analysis is extended till the control displacement for which λ = 0.

239 It is worth highlighting that, if active, the effect of friction gradually decreases after a certain displacement, due to the
240 progressive detachment of the corner. The variation of the frictional forces can be represented by a non-linear function of the
241 decreasing number of involved rows, similarly to the rocking façade, extensively described in [15].
242 The pushover curves can be constructed with reference to the forces and displacements belonging to the plane of rotation.
243 Nevertheless, when the seismic capacity should be compared with the seismic demand represented in given directions, the
244 curves can also be represented as their projections in different planes, as shown for the case study in Section 4.
245

246 **3. NON-LINEAR DYNAMIC ANALYSIS OF ROCKING CORNERS**

247 The non-linear dynamic analysis is the second method here proposed to assess the structural safety of masonry rigid blocks
248 under earthquake ground motions. The two methods have in common the assumption that local mechanisms of masonry
249 buildings can be idealized as kinematic chains of macro-block assemblages. The main difference with respect to the non-
250 linear static analysis lies in the fact that the dynamic analysis considers the evolution of motion over time, not neglecting the
251 dynamic response that can be decisive especially for near-fault ground motions. The great potential of the dynamic analysis
252 also consists in considering the energy dissipation over each impact, which is a phenomenon intrinsically connected to the
253 dynamic motion of rigid objects. As opposed to the non-linear static analysis, which is based on the non-standard limit analysis
254 when frictional resistances are taken into account, the way of considering seismic excitation is different. Indeed, in the non-
255 linear static analysis the horizontal static actions are assumed as a percentage of the gravity loads through a load factor applied
256 to the centre of mass of each macro-block. In the dynamic analysis, the seismic input is assigned as acceleration time-history
257 at the base of the block, and the response is obtained by the resolution of the equation of motion. In this way, the real seismic
258 input is considered, not some intensity measures, such as Peak Ground Acceleration, Peak Ground Velocity or Displacement,
259 Arias Intensity etc, which often cannot be significant or exhaustive for the problem under consideration.
260 The main parameters describing the rigid block are the radius vector, a segment connecting the pivot point to the centre of
261 mass and providing a measure of the size, and the slenderness ratio, which also has a strong influence in the dynamic response.
262 The foundation on which the block rocks is assumed rigid, whereas different horizontal restraints, e.g. tie-rods or transverse
263 walls, can be considered.
264 When the rigid block under consideration is the rocking corner of a masonry building, these aspects can be considered in a
265 similar way by selecting an appropriate prismatic block equivalent to the complex geometry of the corner. The equivalent
266 foundation will be therefore located at a certain height of the masonry structure. For this reason, a proper amplification of the
267 ground motion has to be introduced by evaluating the dynamic properties of the whole building.

By using the displacement-based method, pushover curves express the capacity of the masonry macro-block, which need to be combined with the acceleration displacement response spectra to allow the seismic verification. By contrast, the outcome computed with the dynamic analysis takes the form of a displacement time-history, whose peak corresponds to the demand. The condition of instability of the rocking motion is represented by the attainment of a rotation angle of 90° (overturning condition).

3.1. Rigid block model

The rigid block model, rocking on a rigid base, follows a specific dynamics of motion, studied for the first time by Housner [4]. This model is intuitive and can be used for assessing the behaviour of masonry elements subjected to out-of-plane failures. The simplest form of the equation of motion, taken from the seminal Housner's work [4], is (Figure 4):

$$I_O\ddot{\vartheta} + \mathrm{sgn}(\vartheta) mgR \sin(\alpha - \mathrm{sgn}(\vartheta)\vartheta) - m\,\ddot{u}_g R \cos(\alpha - \mathrm{sgn}(\vartheta)\vartheta) = 0 \quad (9)$$

where I_O is the polar inertia moment with respect to the oscillation point O, $I_O = \frac{4}{3}m(h^2 + t^2) = \frac{4}{3}mR^2$, and $\ddot{u}_g$ is the acceleration time-history. The model, with lumped mass m concentrated in the center of mass of the block, does not consider either sliding nor bouncing, hypothesis that is acceptable when the slenderness of the block is greater than 3 [32]. The damping of the non-linear dynamic model is represented by the energy dissipation at each impact of the pivot points O or O' on the ground. This is computed by reducing the velocity of rotation immediately after the impact through a reduction factor called "coefficient of restitution", function of the slenderness angle α [4].

As for the restraints, in general three configurations are possible, as shown in Figure 4:

a) free rocking block in bilateral or two-sided motion (2S), Figure 4a and Eq. (9);
b) block horizontally restrained by a concentrated spring with stiffness K, simulating a steel tie-rod (Figure 4b);
c) block horizontally restrained by a spring bed with stiffness K', simulating the transversal walls (Figure 4c).

Among the three scenarios, the restrained ones are considered when dealing with masonry corners or masonry walls interacting with roofs [14]. In particular, for a realistic modelling, the unilateral or one-sided rocking (1S) should be preferred to the two-sided (2S) one; in fact, for instance, if a steel tie-rod is the only active horizontal restraint, the effect of tying has to be assumed only when the tie-rod is in tension (Figure 4b), and therefore only in one direction of motion.

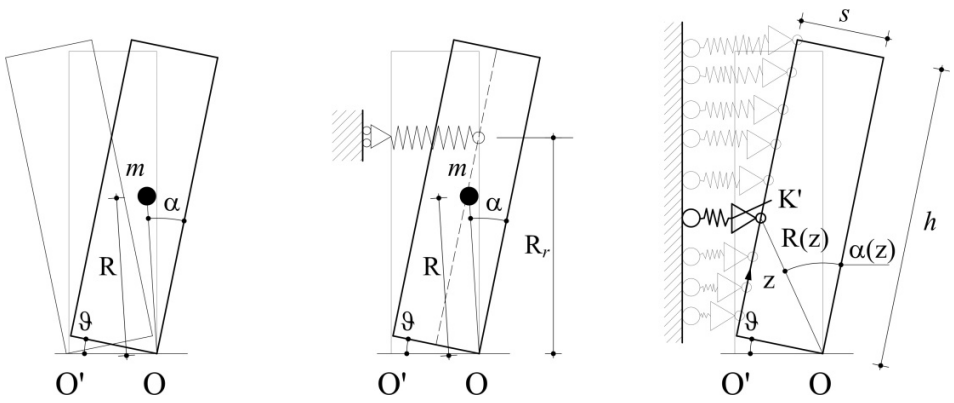

Figure 4 Housner's original block, bilateral or two-sided (2S) rotation (a), one-sided (1S) rotation of the block restrained by a single spring (b) and by a spring bed (c).

So, the activation of the horizontal restraints depends on the clockwise or counter-clockwise direction of the rocking motion. (Figure 5). In 1S, the spring or spring bed stiffness is therefore different in the two directions of rotation. The problem is inherently non-linear even in the free condition due to the dependency of the terms in the equation of motion on trigonometric functions.

When the spring is compressed, one calls its stiffness K_c (single spring, in [F/L]) or K'_c (spring bed, in [F/L^2]).

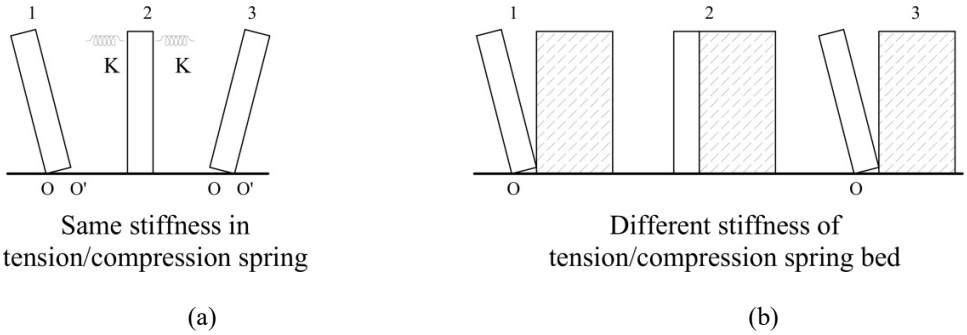

Figure 5 Two-sided (2S) motion (a) and one-sided (1S) motion (b).

306 The spring bed stiffness in compression K'_c can be estimated with the following expression [26]:

$$K'_c = \frac{E_x A}{L h} = E_x \frac{t_t}{L} \tag{10}$$

307 where E_x is the masonry elastic modulus in the horizontal direction, t_t and L respectively are the thickness and effective length
308 of the transversal walls, whereas $A = t_t h$ is their cross section. Eq. (10) is only valid if the spring bed is active along the whole
309 height of the block h (Figure 4c). In the opposite direction of rotation, the transversal walls can react by holding the rocking
310 wall. Besides, although difficult to estimate, a spring bed in tension could be taken into account by considering the frictional
311 resistances discussed in §2.1, in order to create a bridge with the kinematic analysis. A first attempt to define possible values
312 of spring bed stiffness in tension K'_t can be found in [33].
313 In summary, the smeared horizontal restraints representative of the transverse walls can be indicated with a stiffness K', that
314 can be equal either to K'_c for the inward rotation (compressed walls) or to K'_t in the outward rotation (walls in tensile state).
315 The steel tie-rods, if any, are supposed to be active only in tension and are modelled as individual springs. Their position is
316 defined through a position coefficient $p = R_r/R$ (Figure 4b) [26], while α_r is the corresponding radius vector.
317 The complete equation of motion is:

$$\begin{aligned} &I_0\ddot{\vartheta} + \mathrm{sgn}(\vartheta) mgR \sin A_\vartheta + \\ &+\mathrm{sgn}(\vartheta)\, K\, p^2 R^2 \cos A_{r,\vartheta} \left[\sin \alpha_r - \sin A_{r,\vartheta}\right] + \mathrm{sgn}(\vartheta)\, K'\, h \left(\bar{A} + \frac{\bar{B}h}{2} + \frac{\bar{C}h^2}{3}\right) - m\, \ddot{u}_g R \cos A_\vartheta = 0 \end{aligned} \tag{11}$$

318 where $A_\vartheta = \alpha - \mathrm{sgn}(\vartheta)\vartheta$ and $A_{r,\vartheta} = \alpha_r - \mathrm{sgn}(\vartheta)\vartheta$. The terms multiplying K' are function of the rotation amplitude ϑ and of
319 the wall thickness s:

$$\begin{aligned} &\bar{A} = \mathrm{sgn}(\vartheta)\, s^2 \sin\vartheta\, \cos\vartheta\, (1 - \cos\vartheta); \\ &\bar{B} = s\, (\sin^2\vartheta\, \cos\vartheta - \cos^3\vartheta + \cos^2\vartheta); \\ &\bar{C} = \mathrm{sgn}(\vartheta) \sin\vartheta\, \cos^2\vartheta \end{aligned} \tag{12}$$

320

321 **3.2. Non-linear dynamic approach**

322 For the analysis of the rocking corner mechanism, the preliminary stage consists in defining an equivalent rectangular block
323 through a specific equivalence criterion. This procedure has the aim of strongly simplifying the rocking analysis of the corner
324 by solving Eq. (11) valid for a prismatic block and converting the 3D motion into an equivalent 2D behaviour.
325 Let us assume the general configuration displayed in Figure 6a,b, defined by the crack configuration described in §2.2: tthe
326 corner is composed by two intersecting walls, one has an opening and the other one is full and both walls are subjected to the

roof overload. A straightforward method to take into account the roof loads regards the assumption of a system of lumped masses. Both walls are characterized by vertical uniformly distributed overloads and their resultants are punctual loads acting on A, B, C points. On point A, also the horizontal thrust of a strut, if any, can be considered.

The steps required to find the equivalent perpendicular block are the identification of the centre of mass, the application points and entities of roof loads and horizontal restraints. The application points of the roof loads are considered as the current ones, without any modification, therefore some of them can fall within the equivalent block (as displayed in Figure 6c).

As already introduced for the non-linear static model, two phases of motion can be distinguished, depending on the state of contact between roof and wall:

- *phase* 1: the corner rocks around the pivot point O bearing the roof loads; G is the barycentre of the system wall and additional roof loads;
- *phase* 2: the corner rocks without the contribution of the roof loads, G_m is the corresponding barycentre.

In *phase* 1, the centre of mass G and the moment of inertia I are obtained by the contribution of masses m, m_A, m_B, m_C.

In *phase* 2, the contribution on the centre of mass G_m and on the moment of inertia I_m are only due to the masonry portion, and therefore to the mass m. *Phase* 2 is reached once that a threshold horizontal displacement of the rocking corner is attained: by assuming that the roof stands in its own position, the contact between masonry corner and wall is not guaranteed anymore. Clearly, the equation of motion is updated considering the transition from *phase* 1 to *phase* 2, with a specific subroutine of the specifically developed MATLAB code.

As described in §2.1, the inclination of the rotation axis ω is orthogonal to line OG during *phase* 1 (Figure 6a). The strategy to consider an equivalent prismatic block is to convert the motion around the ω axis into two components along the main building directions (X and Y in Figure 6). The equivalent half-thickness of the wall, say in X-direction (rotation around Y-axis), is the X-coordinate of G. From it, the equivalence with the inertia moment corresponding to the real geometry of the corner gives the equivalent block height h_{eq}.

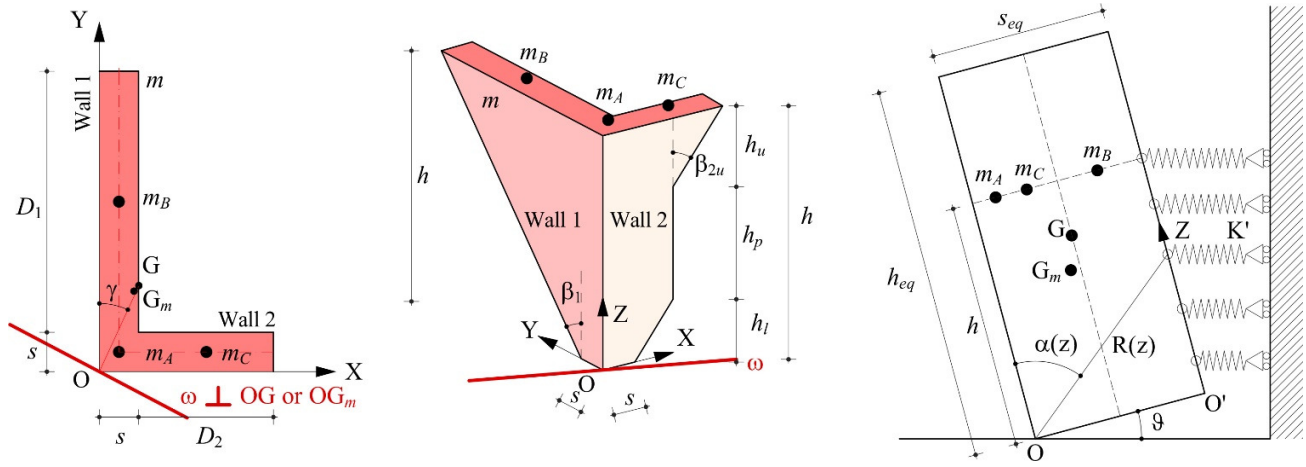

(a) (b) (c)

Figure 6 In-plan view of the corner mechanism (a), 3D view (b) and equivalent rectangular block (c) with the indication of the roof masses.

As for the boundary conditions, one-sided motion can be considered with a spring bed stiffness K′ representative of the transverse walls. In the inward direction and in the outward direction of rotation, respectively a compression and a tension spring bed stiffness can be defined according to what introduced in §3.1.

To correctly take into account these boundary conditions with respect to the rotation axis ω, the stiffness has to be considered in the direction orthogonal to the rotation axis (K'_X and K'_Y) in such a way to include it in the equivalent mechanism (Figure 6c) [20]. More in detail, when the rotation axis is X (Y), only the stiffness K'_Y (K'_X) is considered. Again, the steel tie-rods, if present, can be considered with a spring of stiffness K acting in the actual application point. Another possible parameter to include in the equation of motion is the roof thrust T_s if any, that can be computed with the method expressed in [14].

The final equation of the rocking corner mechanism is therefore:

$$I_\omega \ddot{\vartheta} + \sum_i \mathrm{sgn}(\vartheta) m_i g R_i \sin \hat{A}_i - \sum_i m_i R_i \cos \hat{A}_i \, \ddot{u}_g g + \mathrm{sgn}(\vartheta) \mathrm{K}' h \left(\bar{A} + \frac{\bar{B}h}{2} + \frac{\bar{C}h^2}{3} \right) + \tag{13}$$

$$+\mathrm{sgn}(\vartheta) \mathrm{K} R_r^2 \cos \hat{A}_r \left[\sin \alpha_r - \sin \hat{A}_r \right] - T_s R_r \cos \hat{A}_r = 0$$

where $\hat{A}_i = \alpha_i - \mathrm{sgn}(\vartheta)\vartheta$, $\hat{A}_r = \alpha_r - \mathrm{sgn}(\vartheta)\vartheta$ and $\bar{A}$, $\bar{B}$, $\bar{C}$ are expressed by Eq. (12).

4. A CASE STUDY ANALYZED WITH THE TWO PREDICTIVE MODELLING APPROACHES

4.1. The case study of a masonry corner collapsed during 2016-2017 Central Italy earthquakes

The case study selected for the corner mechanism analysis is the primary school P. Capuzi in the municipality of Visso (Macerata, Central Italy), which was subjected to the seismic events of the 2016-17 Central Italy earthquake (Figure 7). The main damage occurred to the masonry building after the seismic shocks of August and October 2016 is the collapse of one corner in a typical out-of-plane mode due to improper connections between the walls and the timber roof. The analytical models described in the previous sections are hereby applied to this case study, to validate their reliability and suitability in the assessment of the seismic safety of the structure.

The building has a T-shape with four levels, three of them above ground (raised ground floor, first floor and attic) and a basement partially sub-grade. The load-bearing masonry walls extend upwards from the basement until the attic and are made of stone masonry (square rubble masonry type), with some parts in clay bricks. The hipped roof has a timber structure consisting of rafters and purlins that are supported by a system of beams or by the inner walls extending until the top of the roof. In correspondence of ridges and valleys, hip rafters are present. The information about geometry, structural configuration and seismic damage was supplied by the Italian Network of University Laboratories in Seismic Engineering (RELUIS) and the University of Genova, in charge of post-earthquake surveys [34]. This source also provided a detailed description of the damage experienced by the building, updated on the date of December 8th, 2016.

(a)

(b)

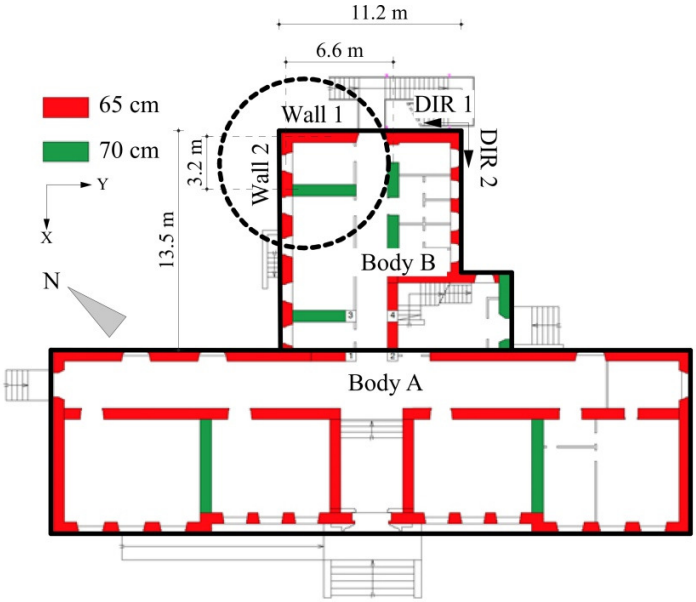

(c)

Figure 7 The P. Capuzi primary school in Visso (Macerata) before (a) and after (b) the 2016-17 Central Italy Earthquakes. Plan view of the first floor with a dashed circle indicating the corner failed (c) [34].

In order to analyze the corner failure, involving the upper level of the building (first floor and attic), it is important to highlight that the thrusting elements of the roof are the hip rafters sitting on the corners of the building along their bisector planes and rising to the central ridges (Figure 8); to each side of these hip rafters a number of purlins, with variable length, are framed parallel to the two intersecting walls, so defining a thrusting point load at about the centre of their intersection area, as described in detail in Appendix A. This means that the weight of the roof around the corner is transferred to the walls in major part through the hip rafter as a concentrated inclined load and in minor part (just the bottom strips of the roof) along the walls as uniformly distributed loads.

The masonry walls of the corner under study are made out of two outer layers of split stones and a rubble inner core, defining a transversal section with thickness s of about 65 cm. The average dimensions of the stone blocks are $l_b = 30$ cm and $h_b = 15$ cm (Figure 2c), while a conventional value of the thickness s_b is herein assumed coincident with that related to the transversal section ($s_b = s$). The blocks are arranged in a quite regular half-running bond pattern, allowing the adoption of the staggering ratio $\tan\alpha_b = l_b/(2h_b) = 1$, i.e. $\alpha_b = 45°$. The blocks are also assembled with mortar of good quality and provide sufficient transversal connections between the outer layers and the core, exhibiting therefore a good monolithic behavior.

Table 1 reports the input data needed for the rocking analysis, together with those sketched in Figure 9. For the sake of simplicity, all overloads are collected in a unique uniformly distributed load applied on the vertical mid-plane of the walls. These overloads include weights transferred by the roof, concrete curb, low wall and horizontal diaphragm indicated in Figure 8b. In particular, the light diaphragm of the attic is assumed to be distributed 80% on Wall 2 and 20% on Wall 1 and W_{s0} is the weight of the concrete curb plus the low wall on the intersection of Walls 1 and 2.

To the end of the application of the two proposed models, the resultant of all the involved masses (the masses of the rocking macro-block and of the roof) was considered applied in the barycenter G or G_m (Figure 2 and Figure 6), depending on the considered phase of motion described in Section 3.2. G or G_m is a hypothetical point where all the involved masses may be assumed to be concentrated and where their weighted relative positions sum to zero. Details of calculation of the centre of mass coordinates for the collapsed corner are reported in Appendix B.

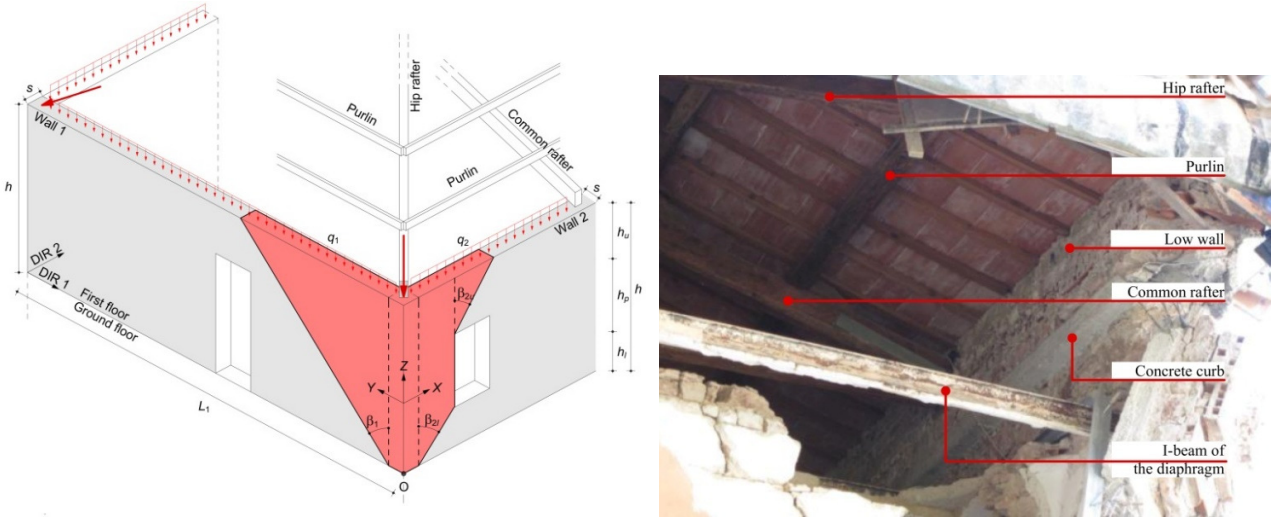

(a) (b)

Figure 8 3D scheme of the school roof and corner (a) and details of other overloads on the walls (b).

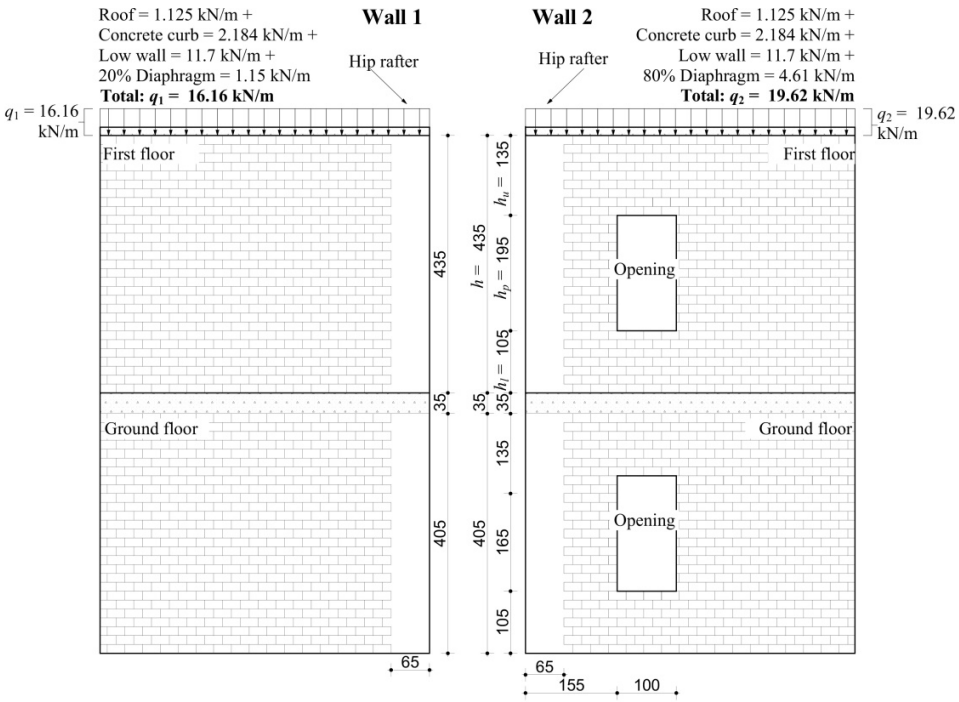

Figure 9 Wall 1 and wall 2 of the failed corner at the first floor, with dimensions in centimetres.

Table 1 Input data for the masonry corner analyzed with kinematic and dynamic analysis.

Geometry		Loadings	
Height [m]	4.35	Specific weight of walls [kN/m^3]	21.00
Thickness of walls (s) [m]	0.65	Weight of half-unit (W_b) [kN]	0.31
Number of rows (n)	29	Weight of the roof (W_r) [kN/m^2]	1.5
		Overloads on Walls 1 and 2 (q_1 and q_2)	16.16 and 19.62
Block size (l_b x h_b) [m]	0.3 x 0.15	[kN/m]	
Inclination angle of the pitches (θ_p) [°]	21	Overload on intersection of Walls (W_{s0}) [kN]	9
Inclination angle of the hip rafter (θ_r) [°]	15.19	Gravity load due to the hip rafter (W_s) [kN]	15.27
Tributary area of the hip rafter (A_p) [m^2]	13.78	Static thrust due to the hip rafter (T_s) [kN]	1.87
Geometrical and mechanical properties of the equivalent rocking block			
	around Y	around X	
s_{eq} [m]	1.308	2.864	
h_{eq} [m]	6.199	6.342	
R_{eq} [m]	3.410	3.640	

α_{eq} [rad]	0.193	0.404
K_c' [N/m^2]	1.57E9	5.49E8
e [-]	0.945	0.771

420

421 **4.1.1. The seismic input and limit states**

422 To analyze the seismic demand for the masonry corner under study, four seismic events of the 2016-2017 Central Italy
423 earthquakes are taken into consideration. These are the first seismic shocks occurred on August 24th 2016 with magnitude
424 M_W = 6.0, when the failure mechanism activated, and the three sequences on October 26th and 30th 2016 with magnitudes
425 M_W = 5.4, 5.9 and 6.5 progressively, approximately when the corner totally collapsed [34].
426 Instead of the records on the ground, the analysis carried out in this paper is referred to the seismic inputs recorded by the bi-
427 axial accelerometer previously placed at the base of the first floor of the building, on the other corner of Body B (Figure 7c
428 and Figure 8a). This is part of the system of accelerometers placed at different levels of the structure by the Seismic
429 Observatory of Structures (OSS) [35] to permanently monitor the building. The acceleration and displacement time-histories
430 obtained by the mentioned sensor for the selected seismic events allow characterization of the seismic input at the base of the
431 corner as direct amplification of the corresponding ground motion.
432 In Table 2 some information about the four seismic events is reported, such as the distance of the school from epicentres, the
433 Peak Ground Acceleration (PGA), Peak Floor Acceleration (PFA) and the amplification factor (PFA/PGA) obtained for the
434 two horizontal components (Dir 1 and Dir 2) sketched in Figure 7c.
435 These events represent the seismic demands for the corner, herein named as displayed in the first column of the table. The
436 data in this table show that the corner was subjected to significant values of horizontal motion; in particular, the highest values
437 of horizontal PFA were recorded during the M_w = 6.5 earthquake of October 30th, which were equal to 0.465g and 0.682g in
438 the 1 (rotation around X, Figure 8a) and 2 (rotation around Y) directions, respectively. This means that the two PGAs of this
439 seismic event were amplified 1.6 and 2.27 times on the first floor of the building, against the average amplification factors of
440 1.54 and 2.02 for Dir 1 and Dir 2, respectively.

441

442 **Table 2 Peak ground and floor accelerations for the four 2016-17 Central Italy seismic events considered.**

Earthquake	Distance from epicentre [km]	Direction	PGA [g]	PFA [g]	Amplification factor
2016/08/24_M_w = 6.0	28	Dir 1	0.33	0.58	1.75

(Demand I-1,2)		Dir 2	0.32	0.61	1.91
2016/10/26_M_w = 5.4	7	Dir 1	0.30	0.47	1.58
(Demand II-1,2)		Dir 2	0.21	0.55	2.61
2016/10/26_M_w = 5.9	4	Dir 1	0.36	0.44	1.23
(Demand III-1,2)		Dir 2	0.47	0.61	1.30
2016/10/30_M_w = 6.5	10	Dir 1	0.29	0.47	1.60
(Demand IV-1,2)		Dir 2	0.30	0.68	2.27

On the other hand, the capacity of the masonry corner should be referred to the equivalent non-linear Single Degree Of Freedom (SDOF) system conventionally representing the motion of the corner in both static and dynamic analysis. In particular, the capacity thresholds are herein represented by three limit states, i.e. LS0, LS1 and LS2, according to the threshold values proposed by Giresini et al. [36]. The first one corresponds to the rocking initiation, which conventionally occurs when the PGA or PFA is greater than or equal to the minimum acceleration that causes rocking. The second one, LS1, is assumed to be a limit state for which the maximum displacement of the control point attains a value of 40% of its ultimate displacement d^*_0, the latter representing the instability displacement under quasi-static loading, also called static instability displacement. This limit state can refer to a moderate rocking with some damages on the structures adjacent to the rocking corner itself. Moreover, LS2 is representative of the near-collapse condition, assumed to be reached when the maximum displacement is 150% of d^*_0. It should be again noticed that, for a rocking wall system, the theoretical maximum limit of rotation is 90° (overturning condition), and that the static limit can be overcome keeping the stability. However, to make comparable the two proposed approaches and for the sake of safety, in this work LS2 is chosen as the reference ultimate limit state. To summarize, for both models the three limit states correspond to the following capacity values at the floor level, respectively in terms of acceleration and displacement:

$$\text{LS0} \rightarrow \quad \text{PFA}_\text{C} = \lambda_0 \text{g} \qquad \text{LS1} \rightarrow \quad d^*_{\text{C1}} = 0.4 d^*_0 \qquad \text{LS2} \rightarrow \quad d^*_{\text{C2}} = 1.5 d^*_0 \tag{14}$$

where λ_0 is the initial load factor given by Eq. (6). In order to compare the results of the two proposed modelling approaches, the values of the parameters λ_0 and d^*_0 in Eq. (14) are derived by the application of the static model and considered valid for the dynamic one, as developed in the following sections for the case under study. The only slight difference is in the PFA_c, which for the static model takes into account the rate of the total mass e^* described in Section 4.2.

The seismic assessment of the rocking masonry corners is thus evaluated by a safety index ζ summarizing the comparison between the expected seismic capacity and demand, with reference to the three LS0, LS1 and LS2 limit states, i.e.:

$$\zeta_{LS0} = \frac{PFA_C}{PFA_D} \qquad \zeta_{LS1} = d^*_{C1}/d^*_D \qquad \zeta_{LS2} = d^*_{C2}/d^*_D \tag{15}$$

where the subscript D indicates the demand. The verification is satisfied if the indexes are greater than unity.

It is worth highlighting that the evaluation of the seismic demand for LS1 and LS2 in terms of displacements is performed by following different procedures for the two modelling approaches. In fact, while the displacement demand for the dynamic model is a direct result of the dynamic equations, the static model requires the superimposition of the capacity curve with the demand ADRS, as described in the following section.

4.2. Application of the non-linear static model

The first step to assess the seismic capacity of the corner under study is the definition of the geometry of the failing wedge by means of the limit analysis procedure described in Section 2, i.e. by minimizing the load factor expressed by Eq. (6) with respect to the two unknown angles of crack on the two intersecting walls. As highlithed in Figure B.1 and Table B.1 of Appendix B, the geometric parameters C_1 and C_2 of the failing wedge are strictly related to these angles in terms of $\tan\beta_1$ and $\tan\beta_{2u}$, respectively, while frictional resistances depend on these angles through Eq. (3).

The procedure is developed for spreadsheet and a multipurpose mathematical programming solver is used to solve the problem of optimum. By assuming the friction coefficient $f = 0.6$, as suitable for stone masonry walls [37–39], the result of the minimum load factor is $\lambda = 0.464$ and the resulting geometry pattern of the moving corner is a wedge characterized by the two angles of crack β_1 and β_{2u} equal to their maximum value given by the half-unit shape, i.e. $\alpha_b = 45°$ (Figure 2c). This means zero frictional resistances provided by Eq. (3) and only activation of pure rotation.

This result is in very good agreement with the actual collapse pattern observed in Figure 7b, where it is evident that the presence of a window in Wall 2 strongly influences the development of the cracks. In fact, these tend to localize near the vertexes of the opening, while a greater portion of Wall 1 is involved. By contrast, the opening in Wall 1 does not affect the configuration of the rocking wedge because quite far from the corner and the inclination of the crack line results to be at its maximum value ($\beta_1 = \alpha_b$).

The values of the forces defining the minimum load factor of Eq. (6) are summarized in Table 3, where W is the sum of all the involved weights reported in Table B.1 of Appendix B. These can also be distinguished in the weight of the failing masonry corner (W_m) and that of the roof (W_q).

Table 3 Forces defining the minimum load factor for the failing masonry corner under study.

Forces	Value [kN]	Horizontal lever arm (xy) [m]	Vertical lever arm (z) [m]
Weight of the failing masonry corner (W_m)	227.17	1.45	2.73
Weight of the roof (W_q)	138.73	1.78	4.35
Resultant of gravity loads (W)	365.9	1.57	3.35
Fricitional resistances (F_i)	0	-	-
Static thrust (T_s)	1.87	-	4.35

Besides, as already stated in §3.2, the evolution of the motion is characterized by two distinct phases, depending on the contact between roof and wall:

- *phase* 1: the corner rotates till the complete unthreading of the roof;
- *phase* 2: the corner rocks without the contribution of the roof loads.

In *phase* 1, the centre of mass G is obtained with the contribution of all the masses involved, as detailed in Appendix B. Its coordinates are derived by Eq. (B.1) to be $x_G = 0.65$, $y_G = 1.43$ and $z_G = 3.35$, while the vertical plane of rotation results to be inclined of $\gamma = 24.54°$ with respect to the YZ-plane, according to Eq. (B.2). In *phase* 2, the new centre of mass G_m is only related to the masonry portion (Figure 6), with new coordinates $x_{Gm} = 0.57$, $y_{Gm} = 1.33$ and $z_{Gm} = 2.73$, while $\gamma_m = 23.24°$ from Eq. (B.3).

However, the pushover curve displayed in Figure 10 is constructed with reference to the control point which is the centre of mass G_m accounting for the masonry portion only (*phase* 2). This curve is obtained using Eqs. (6) and (8) for increasing angle of rotation ϑ (Figure 3). Moreover, it is referred to the capacity along the plane of rotation that is orthogonal to the rotation axis ω (Figure 2). As shown in Figure 10, the transition from *phase* 1 to *phase* 2 is expected to occur at the displacement $d_{G0} = 0.49$ m, calculated using Eq. (8).

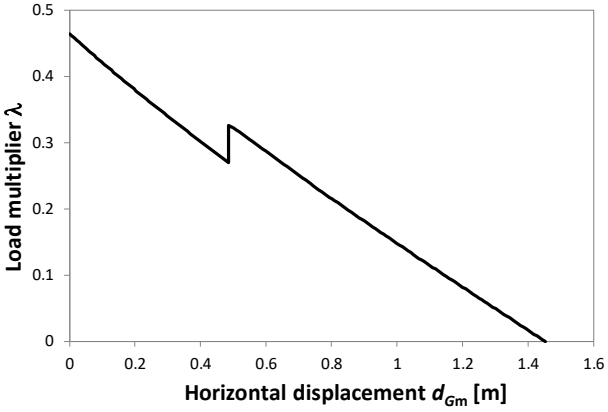

506

507 **Figure 10 Pushover curve of the collapsed corner in the masonry school building under study.**

508

509 According to the Capacity Spectrum Method [23,40], the capacity curve of the equivalent non-linear SDOF system is derived
510 from the pushover curve by assuming:

$$a^* = \frac{\lambda g}{e^*} \qquad d^*_{Gm} = \Gamma\, d_{Gm} \tag{16}$$

511 where, e^* is the rate of the total mass that participates to the rocking mechanism and Γ is the transformation factor of the
512 displacements. Being $\delta_{x,j}$ the virtual horizontal displacement of the j-th lamping mass, the two introduced factors are:

$$e^* = \frac{\left(\sum_j W_j \delta_{x,j}\right)^2}{\sum_j W_j \ \sum_j W_j \delta^2_{x,j}} \qquad \Gamma = \frac{\sum_j W_j \delta^2_{x,j}}{\delta_{x,Gm} \sum_j W_j \delta_{x,j}} \tag{17}$$

513 which assume different values for each of the two phases of motion. In fact, taking into account the values in Table 3, these
514 factors are equal to unity when only the masonry portion is involved in the mechanism (*phase* 2), while e^* = 0.95 and Γ = 1.29
515 for the whole *phase* 1, as reported in Table 4.

516

517 **Table 4 Factors to define the SDOF system in the two phases of motion.**

Factors (Eq. (17))	Phase 1	Phase 2
$e^* = \frac{\left(W_m z_m + W_q z_q\right)^2}{W\left(W_m z_m^2 + W_q z_q^2\right)}$	0.95	1
$\Gamma = \frac{W_m z_m^2 + W_q z_q^2}{z_m\left(W_m z_m + W_q z_q\right)}$	1.29	1

518

The seismic capacity and demand of the static model are then superimposed in terms of acceleration a^* and displacement d^*_{Gm} of the equivalent non-linear SDOF system, with reference to the two directions of the available seismic inputs recorded by the bi-axial accelerometer (Figure 11). To this aim, the capacity is represented by the two components of acceleration and displacement along the Directions 1 and 2, given by the following expressions:

$$a_1^* = a^* \cos\gamma \qquad d_{1,Gm}^* = d_{Gm}^* \cos\gamma \qquad \text{for Dir 1}$$
$$a_2^* = a^* \sin\gamma_m \qquad d_{2,Gm}^* = d_{Gm}^* \sin\gamma_m \qquad \text{for Dir 2} \tag{18}$$

The resulting capacity curves obtained using Eq. (16) for increasing angle of rotation ϑ (Figure 3) are almost straight lines, with different initial accelerations (a^*_0) and final displacements (d^*_0). In fact, $a^*_{0,1} = 4.37$ m/s^2 and $d^*_{0,1} = 1.33$ m for DIR 1, while $a^*_{0,2} = 2$ m/s^2 and $d^*_{0,2} = 0.57$ m for DIR 2. The change from *phase* 1 to *phase* 2 is also indicated in the figures for both directions.

On the other hand, the demand of the available seismic inputs is expressed in terms of overdamped elastic ADRS, by applying a damping correction factor η, like the one proposed by Eurocode 8 [41]:

$$\eta(T) = \sqrt{\frac{10}{5 + \xi(T)}} \tag{19}$$

where an equivalent viscous damping $\xi = 5\%$ ($\eta = 1$) is assumed.

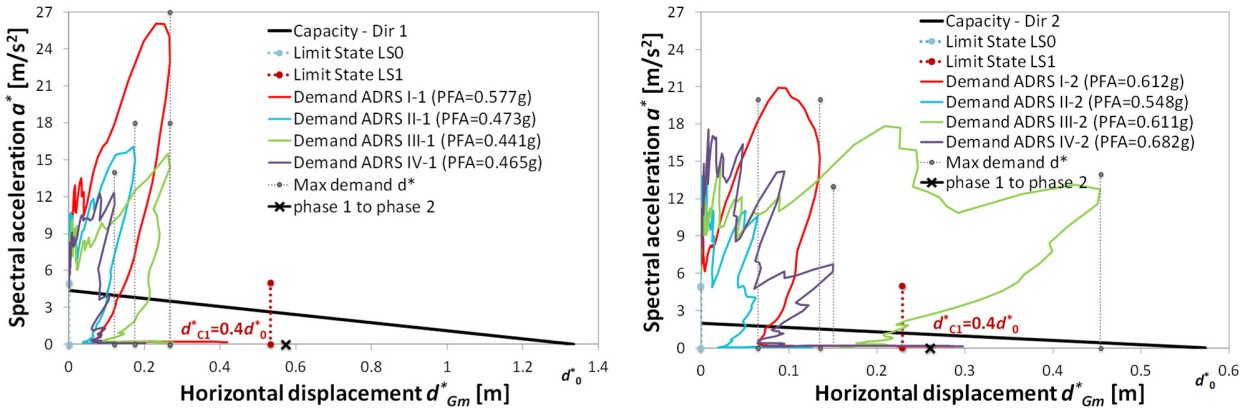

(a) (b)

Figure 11 Evaluation of the displacement demand of the rocking corner by means of the non-linear static model, for Direction 1 (a) and Direction 2 (b).

The capacity thresholds are represented by the three LS0, LS1 and LS2 limit states expressed by Eq. (14), which are the same for the two presented models. It is worth highlighting that the LS1 limit state is close to the first threshold horizontal displacement (*phase* 1 to *phase* 2) for both directions, corresponding to the complete unthreading of the roof. This means that

for this case study the LS1 limit state substantially represents this threshold. The three limit states of Eq. (14) are reported in Table 5 for the direction of the plane of rotation, which is orthogonal to ω, and for DIR 1 and DIR 2 as functions of the angle γ or γ_m, according to Eq. (18**)**.

From Figure 11 and Table 5, it is first evident that the most vulnerable direction is DIR 2 with the lowest capacity both in terms of acceleration and displacement and with most demanding input represented by the $M_w = 5.9$ earthquake of October 26th (Table 2). This first result is in perfect agreement with the actual collapse occurred just after this input, as clearly indicated by the survey reports [34,42].

Table 5 Seismic capacity for the three limit states LS0 (mechanism activation), LS1 (moderate rocking) and LS2 (near-collapse).

	LS0 - PFA_C [g]	LS1 - d^*_{C1} [m]	LS2 - d^*_{C2} [m]
DIR ⊥ ω	0.49	0.58	2.18
DIR 1	0.45	0.53	2.00
DIR 2	0.20	0.23	0.86

4.3. Application of the non-linear dynamic model

The geometry of the rocking corner defined by the non-linear static analysis is assumed to be the same for the application of non-linear dynamic analysis. The validity of this assumption can be found in the parametric analysis performed in [Giresini et. Al. 2019 che è l'attuale citazione [20] One-sided rocking motion…].

Based on this geometry, the rocking analysis is performed by considering an equivalent prismatic block characterized by an equivalent radius vector R_{eq}, between 3.41 m and 3.64 m and slenderness angle α between 0.193 and 0.404 according to the rotation axis (Table 1). The corresponding coefficients of restitution, calculated according to Housner [4], are between 0.77 and 0.95. The mechanical parameters associated with the boundary conditions are the compression spring bed stiffness around X and Y (§3.2) that simulate the transverse walls. The larger value is for the compressive stiffness when the inward rotation is around Y, equal to 1.57E9 N/m^2, greater than the orthogonal value of 5.49E8 N/m^2 [20]. This is due to the fact that the effective length of the transverse wall in X direction is lower because of the presence of the opening. Moreover, null tension spring bed stiffness is assumed in accordance with the non-activation of frictional resistances obtained by the static analysis.

561 However, this assumption may imply more rebound effects in the free direction of rotation (e.g. in negative Y direction if the
562 rotation around X axis is assumed, Figure 6a), which could indeed cause the overturning of the rigid block [25].
563 The results of the rocking analyses are reported in Table 6 for each limit state only for the most vulnerable direction DIR 2,
564 which is the most vulnerable also in the rocking analysis with the higher demand. It is important to notice that the peak
565 displacement caused by the earthquake of October 26th - that actually caused the collapse – is the greatest and equal to 36 cm.
566 However, it should be also pointed out that the numerical analysis did not gather the overturning of the block with this seismic
567 record (namely, it did not reach a rotation of 90° in the time-history). The second most vulnerable earthquake is the first of
568 seismic swarm, the M_w = 6.0 earthquake of August 24th, that indeed probably formed the cracks during the ground motion but
569 did not determine the instability of the corner. In this case, the peak displacement suggested by the rocking analysis is 29 cm,
570 quite close to the previous value, although the PGA is significantly lower (0.32g against 0.47g) and the epicentre was further
571 away (29 km against 4 km), as shown in Table 2.
572 It is again pointed out that, for the dynamic analysis outcomes, the demand is the same for limit states LS1 and LS2, since the
573 demand is defined as the peak of the displacement time-history, which is unique for each seismic record.
574

575 **Table 6 Seismic demand for the three limit states LS0 (mechanism activation), LS1 (moderate rocking) and LS2**
576 **(near-collapse).**

	LS0 - PFA_D [g]	LS1 - d_D* [m]	LS2 - d_D* [m]
Demand I-2	0.61	0.29	0.29
Demand II-2	0.55	0.01	0.01
Demand III-2	0.61	0.36	0.36
Demand IV-2	0.68	0.07	0.07

577

578 ## 5. COMPARISONS BETWEEN THE TWO PROPOSED MODELS

579 The results of the non-linear static and dynamic analyses, here only referred to the most vulnerable DIR 2, can be discussed
580 in terms of a) limit states, b) seismic input and c) seismic safety index, as summarized in Table 7.
581 From these results it is evident that the static model proves to be always more conservative than the dynamic model for the
582 onset of the mechanism and for the other limit states, with the exception of LS1 and LS2 of the Demand I-2, e.g. the M_w = 6.0
583 earthquake of August 24th. This is the first earthquake of the seismic swarm that most likely caused the formation of the

584 diagonal cracks in the masonry walls and therefore the corner geometry. The results confirm that both models can capture the
585 activation of the motion (LS0) occurred for this input, since the safety factors are much less than unity in both directions.
586 However, this earthquake had a low seismic demand in terms of displacement and could not cause the collapse of the corner
587 (Figure 11).
588 Even the subsequent $M_w = 5.4$ earthquake of October 26th (Demand II-2) with its lowest demand but greater amplification
589 factor (Table 2) could only add more damage to the corner without causing its collapse. Instead, the limit state of moderate
590 rocking (LS1) was reached for the second main shock of October 26th (Demand III-2) and, due to the cumulative damage, the
591 corner eventually collapsed. The predictions of the two models are in good agreement with this event, because the safety
592 factors for LS2 state slightly greater than unity do neglect the progressive damaged actually undergone by the masonry
593 structure. As for the comparison of seismic demands, one can notice that between static and dynamic models the first one is
594 not affected by the PGV value of the seismic record, which is instead a relevant seismic intensity measure influencing the
595 stability of an oscillating block. For this reason, it can be observed from Table 7 that Demand I-2 implies a greater seismic
596 demand for the dynamic model than that for the static model, since its PGV is of medium-high intensity (PGV=56 cm/s). In
597 addition, the seismic demands are greater for higher PGA values (comparisons between Demands I-2 and II-2 and between
598 Demands III-2 and IV-2 in Table 2).
599 Comparing the safety indexes of the outcomes of the two approaches, one can observe that the results of the static analysis
600 are "smoother", with values close to unity (with the exception of $\zeta = 13.26$ for Demand II-2). By contrast, when the block is
601 stable for the rocking analysis, due to its strongly reduced motion, the demand, that is the peak response, may be so low that
602 the safety index becomes extremely high (e.g. 22.91, 85.91 for Demand II-2).
603 However, the good predictions of the onset and overturning of the rocking masonry corner selected as a real case study, allow
604 considering the two presented approaches in static and dynamic fields as reliable and efficient modelling strategies, capable
605 to be easily extended to any kind of local failure in masonry buildings and useful to practitioners as well.
606
607 **Table 7 Seismic demands and safety indexes for LS0, LS1 and LS2 in DIR 2.**

		Seismic Demand		Seismic safety index ζ	
		Static Model	Dynamic Model	Static Model	Dynamic Model
Demand I-2	LS0 [g]	0.62	0.61	0.33	0.33
	LS1 [m]	0.14	0.29	1.70	0.79

	LS2 [m]	0.14	0.29	6.36	2.96
Demand II-2	LS0 [g]	0.56	0.55	0.36	0.37
	LS1 [m]	0.06	0.01	3.54	22.91
	LS2 [m]	0.06	0.01	13.26	85.91
Demand III-2	LS0 [g]	0.62	0.61	0.33	0.33
	LS1 [m]	0.45	0.36	0.50	0.64
	LS2 [m]	0.45	0.36	1.89	2.39
Demand IV-2	LS0 [g]	0.69	0.68	0.30	0.30
	LS1 [m]	0.15	0.07	1.52	3.27
	LS2 [m]	0.15	0.07	5.71	12.27

6. CONCLUSIONS

This work presented the analysis of a typical out-of-plane failure mode in masonry buildings with two complementary approaches: the non-linear static and the non-linear dynamic methods. The first one, considering the frictional resistances, is able to predict with a high degree of precision the collapse load factor that activates the incipient mechanism and the capacity curve in terms of displacements, to compare with the seismic demand. The non-linear dynamic analysis considers the evolution of one-sided motion over time by taking into account the influence of transverse walls and energy dissipation under the real seismic record. The two methodologies have been here specialized for considering the corner mechanism, very frequent in masonry buildings subjected to earthquakes especially when the interaction with a thrusting roof is present.

The seismic assessment of a corner mechanism formed in a school building, subjected to the seismic swarm occurred in Central Italy in 2016-2017, was carried out with reference to three limit states, i.e. rocking initiation (LS0), moderate rocking (LS1) and near-collapse (LS2) conditions, being LS0 and LS1 representative of serviceability limit states, while LS2 was considered as an ultimate limit state.

The comparison of results showed a good agreement of the models with the real behaviour of the rocking structure and with each other, even if the static model appears to be more conservative than the dynamic model. In particular, both models were capable to provide a reliable prediction both of the activation of motion for the corner and of its complete collapse. The latter occurred during the most demanding earthquake in terms of displacement of the seismic events of the 2016-17 Central Italy sequence.

626 The accuracy of the assessment methods in predicting the seismic response of the rocking corner under study may guarantee
627 their potential and suitability to be applied to any kind of masonry structural or non-structural element with reference to
628 different geometries, constraints and performance levels.
629

630 **ACKNOWLEDGMENTS**

631 The authors acknowledge the sponsorship of the Italian Civil Protection, through the RELUIS Project – Line: Masonry
632 Structures.
633

634 **APPENDIX A. Calculation of the load transferred by the hip rafter to the corner in the case study building**

635 In order to define the static action that the hip rafter exerts on the intersecting walls, the isostatic scheme shown in Figure A.1
636 is adopted. According to this scheme, it is assumed that the action R_b provided by the ridge beam on the hip rafter is oriented
637 orthogonally to it. It is worth noting that, although this assumption is a great simplification of the more complex connection,
638 it represents a reliable condition between the bounding vertical and horizontal orientations of the ridge support. A linear
639 distributed load, increasing towards the corner, represents the vertical load transferred by the purlins to the hip rafter. The
640 resultant of this load is $Q_p = (A_p \times W_r)/\cos\theta_p$, being A_p and W_r the tributary area and the weight of a square meter of the roof,
641 respectively, and θ_p the inclination angle of the pitches.
642 Hence, the horizontal and vertical components of the reaction of the hip rafter are respectively T_s and W_s; according to the
643 assumed static scheme, they depend on the inclination θ_p as follows:

$$T_s = \frac{1}{3} Q_p \sin\theta_r \cos\theta_r; \qquad W_s = Q_p \frac{3 - \cos^2\theta_r}{3} \tag{A.1}$$

644 where θ_r is the inclination angle of the hip rafter, depending on θ_p through the expression:

$$\theta_r = \tan^{-1} \frac{\tan\theta_p}{\sqrt{2}} \tag{A.2}$$

645

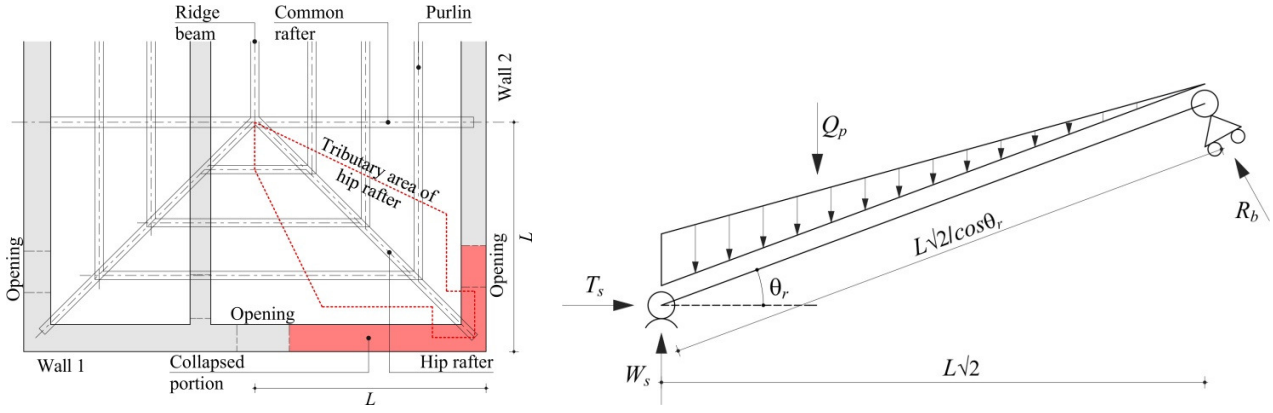

Figure A.1 Layout of the structure of the wooden roof (a) and static scheme of the hip rafter (b).

APPENDIX B. Calculation of the centre of mass coordinates of the collapsed corner of the case study building

The masses involved in the mechanism of the corner are represented in Figure B.1 by the self-weights of the portions of the walls (W_0, W_1, W_{2l}, W_{2p}, W_{2u}), the resultants (W_{s0}, W_{s1}, W_{s2}) of the uniformly distributed overloads and the vertical action of the hip rafter (W_s). In particular, W_{s0} is the weight of the concrete curb plus the low wall on the intersection of Walls 1 and 2, as also reported in Table 1 and Figure 9. The formulations of these forces and the coordinates of their application points are reported in Table B.1. It is worth highlighting that C_1 and C_2 are functions of the two variables $\tan\beta_1$ and $\tan\beta_{2u}$, respectively.

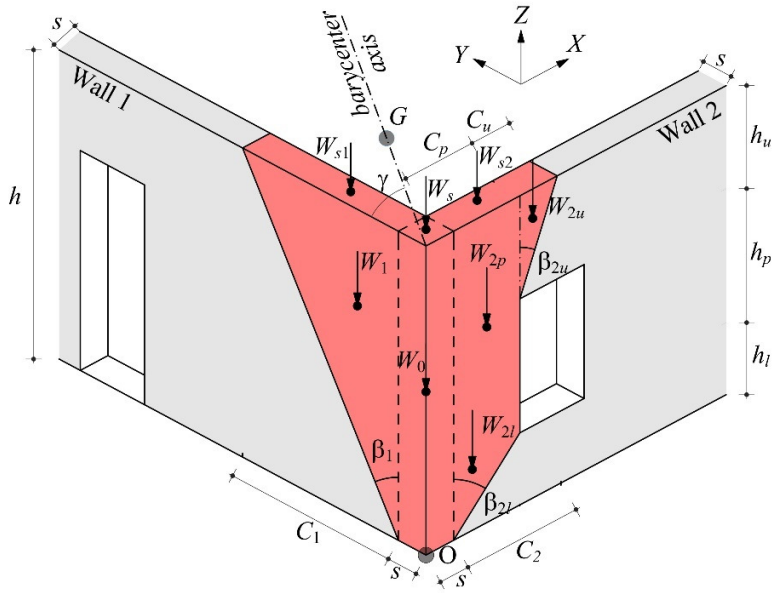

Figure B.1 Axonometric view showing the all the weights involved in the corner mechanism.

Table B.1: Involved weights with the coordinates of their application points

Involved weights	x_j	y_j	z_j
$W_0 = \gamma s^2 H$	$s/2$	$s/2$	$H/2$
$W_s = Q_p \frac{3 - \cos^2\theta_r}{3}$	$s/2$	$s/2$	H
$W_{s0} =$ overload on intersection of Walls	$s/2$	$s/2$	H
$W_1 = 0.5\gamma C_1 H s$	$s/2$	$s + C_1/3$	$2H/3$
$W_{s1} = q_1 C_1$	$s/2$	$s + C_1/2$	H
$W_{2l} = 0.5\gamma C_p h_l s$	$s + C_p/3$	$s/2$	$2h_l/3$
$W_{2p} = \gamma C_p (h_p + h_u) s$	$s + C_p/2$	$s/2$	$h_l + (h_p + h_u)/2$
$W_{2u} = 0.5\gamma C_u h_u s$	$s + C_p + C_u/3$	$s/2$	$H - h_u/3$
$W_{s2} = q_2 C_2$	$s + C_2/2$	$s/2$	H

The cordinates of the centre of mass G or G_m, depending on the considered phase of motion described in Section 3.2, are:

$$x_{G,G_m} = \frac{\sum_j (W_j x_j)}{\sum_j W_j}; \qquad y_{G,G_m} = \frac{\sum_j (W_j y_j)}{\sum_j W_j}; \qquad z_{G,G_m} = \frac{\sum_j (W_j z_j)}{\sum_j W_j} \tag{B.1}$$

For the first phase of motion, the inclination of the vertical plane of rotation with respect to YZ-plane, denoted γ in Figure 2b and Figure B.1, is expressed as:

$$\gamma = \tan^{-1} \frac{x_G}{y_G} \tag{B.2}$$

which still depends on the two variables of the optimization problem.

The solution procedure detailed in Section 4.2 provides the values of $\tan\beta_1$ and $\tan\beta_{2u}$ which minimize the load factor and define the whole geometry of the failing corner. Once defined this geometry, the coordinates of the centre of mass G_m is provided by Eq. (B.1), while the new inclination of the vertical plane of rotation γ_m can be found similarly to Eq. (B.2), i.e.:

$$\gamma_m = \tan^{-1} \frac{x_{G_m}}{y_{G_m}} \tag{B.3}$$

REFERENCES

1. Alecci V, Stipo G, La Brusco A, De Stefano M, Rovero L. Estimating elastic modulus of tuff and brick masonry: A comparison between on-site and laboratory tests. *Construction and Building*

Materials 2019; **204**: 828–838.
2. Griffith MC, Magenes G, Melis G, Picchi L. Evaluation of out-of-plane stability of unreinforced masonry walls subjected to seismic excitation. *Journal of Earthquake Engineering* 2003; **7**: 141–169. DOI: 10.1007/s00264-017-3709-6.
3. Heyman J. The stone skeleton. *International Journal of Solids and Structures* 1966; **2**(2): 249–279. DOI: 10.1016/0020-7683(66)90018-7.
4. Housner GW. The behavior of inverted pendulum structures during earthquakes. *Bulletin of the Seismological Society of America* 1963; **53**(2): 403–417. DOI: 10.1017/CBO9781107415324.004.
5. Pantò B, Giresini L, Sassu M, Caliò I. Non-linear modeling of masonry churches through a discrete macro-element approach. *Earthquake and Structures* 2017; **12**(2): 223–236.
6. Giresini L, Sassu M, Butenweg C, Alecci V, De Stefano M. Vault macro-element with equivalent trusses in global seismic analyses. *Earthquake and Structures* 2017; **12**(4): 409–423. DOI: 10.12989/eas.2017.12.4.409.
7. Andreini M, De Falco A, Giresini L, Sassu M. Collapse of the historic city walls of Pistoia (Italy): Causes and possible interventions. *Applied Mechanics and Materials* 2013; **351**–**352**: 1389–1392.
8. Casapulla C, Giresini L, Lourenço PB. Rocking and kinematic approaches for rigid block analysis of masonry walls: State of the art and recent developments. *Buildings* 2017; **7**(3). DOI: 10.3390/buildings7030069.
9. Sorrentino L, D'Ayala D, de Felice G, Griffith MCC, Lagomarsino S, Magenes G, *et al.* Review of out-of-plane seismic assessment techniques applied to existing masonry buildings. *International Journal of Architectural Heritage* 2016; **11**(1): 2–21. DOI: 10.1080/15583058.2016.1237586.
10. Ferreira TM, Costa AA, Costa A. Analysis of the out-of-plane seismic behavior of unreinforced masonry: a literature review. *International Journal of Architectural Heritage* 2015; **9**(8): 949–972. DOI: 10.1080/15583058.2014.885996.
11. Godio M, Beyer K. Evaluation of force-based and displacement-based out-of-plane seismic assessment methods for unreinforced masonry walls through refined model simulations. *Earthquake Engineering & Structural Dynamics* 2019; **48**(4): 454–475. DOI: https://doi.org/10.1002/eqe.3144.
12. Mistretta F, Stochino F, Sassu M. Structural and thermal retrofitting of masonry walls: An integrated cost-analysis approach for the Italian context. *Building and Environment* 2019; **155**: 127–136.
13. Sassu M, Stochino F, Mistretta F. Assessment method for combine structural and energy retrofitting in masonry buildings. *Buildings* 2017; **7**(71).
14. Giresini L, Fragiacomo M, Sassu M. Rocking analysis of masonry walls interacting with roofs. *Engineering Structures* 2016; **116**: 107–120.
15. Casapulla C, Argiento LU. The comparative role of friction in local out-of-plane mechanisms of masonry buildings. Pushover analysis and experimental investigation. *Engineering Structures* 2016; **126**: 158–173. DOI: 10.1016/j.engstruct.2016.07.036.
16. Walsh K, Dizhur D, Giongo I, Derakhshan H, Ingham J. Predicted versus experimental out-of-plane force-displacement behaviour of unreinforced masonry walls. *Structures* 2018; **15**: 292–306.
17. D'Ayala D, Speranza E. Definition of collapse mechanisms and seismic vulnerability of historic masonry buildings. *Earthquake Spectra* 2003; **19**(3): 479–509. DOI: 10.1193/1.1599896.
18. Speranza E. An integrated method for the assessment of the seismic vulnerability of historic buildings. Ph.D. Thesis, University of Bath, UK, 2003.
19. Casapulla C, Maione A, Argiento LU, Speranza E. Corner failure in masonry buildings: An updated macro-modeling approach with frictional resistances. *European Journal of Mechanics,*

A/Solids 2018; **70**: 213–225. DOI: 10.1016/j.euromechsol.2018.03.003.
20. Giresini L, Solarino F, Paganelli O, Oliveira DV, Froli M. One-sided rocking analysis of corner mechanisms in masonry structures: influence of geometry, energy dissipation, boundary conditions. *Soil Dynamics and Earthquake Engineering* 2019: in press.
21. Casapulla C, Maione A. Experimental and analytical investigation on the corner failure in masonry buildings: interaction between rocking-sliding and horizontal flexure. *International Journal of Architectural Heritage* 2018. DOI: 10.1080/15583058.2018.1529206.
22. Lagomarsino S. Seismic assessment of rocking masonry structures. *Bulletin of Earthquake Engineering* 2015; **13**(1): 97–128. DOI: 10.1007/s10518-014-9609-x.
23. Freeman SA. Development and use of capacity spectrum method. *Proceedings of the 6th US NCEE Conference on Earthquake Engineering/EERI* 1998(Paper 269): 12.
24. Giresini L, Fragiacomo M, Lourenço PB. Comparison between rocking analysis and kinematic analysis for the dynamic out-of-plane behavior of masonry walls. *Earthquake Engineering and Structural Dynamics* 2015; **44**(13): 2359–2376. DOI: 10.1002/eqe.2592.
25. Giresini L. Design strategy for the rocking stability of horizontally restrained masonry walls. In: M. Papadrakakis MF, editor. *COMPDYN 2017 6th ECCOMAS Thematic Conference on Computational Methods in Structural Dynamics and Earthquake Engineering*, Rhodes Island, Greece: 2017.
26. Giresini L, Sassu M. Horizontally restrained rocking blocks: evaluation of the role of boundary conditions with static and dynamic approaches. *Bulletin of Earthquake Engineering* 2017; **15**(1): 385–410. DOI: 10.1007/s10518-016-9967-7.
27. Lagomarsino S, Cattari S. PERPETUATE guidelines for seismic performance-based assessment of cultural heritage masonry structures. *Bulletin of Earthquake Engineering* 2015; **13**(1): 13–47. DOI: 10.1007/s10518-014-9674-1.
28. Drucker DC. Coulomb friction, plasticity and limit loads. *Arm Serv Techn Inf Cent* 1953; **2902**(85): 1–16.
29. Livesley RK. Limit analysis of structures formed from rigid blocks. *International Journal for Numeridal Methods in Engineering* 1978; **12**(12): 1853–1871.
30. Casapulla C, Maione A. Modelling the dry-contact interface of rigid blocks under torsion and combined loadings: Concavity vs. convexity formulation. *International Journal of Non-Linear Mechanics* 2018; **99**: 86–96. DOI: 10.1016/j.ijnonlinmec.2017.11.002.
31. Casapulla C, Argiento LU. In-plane frictional resistances in dry block masonry walls and rocking-sliding failure modes revisited and experimentally validated. *Composites Part B: Engineering* 2018; **132**: 197–213. DOI: 10.1016/j.compositesb.2017.09.013.
32. Lipscombe PR, Pellegrino S. Free rocking of prismatic blocks. *Journal of Engineering Mechanics* 1993; **119**(7): 1387–1410. DOI: 10.1061/(ASCE)0733-9399(1993)119:7(1387).
33. Casapulla C, Giresini L, Argiento LU, Lagomarsino S. Incremental static and dynamic analyses of the out-of-plane response of a masonry church damaged by 2016-2017 Central Italy Earthquakes - Analisi statiche e dinamiche incrementali per la valutazione della risposta fuori piano della facciata di una chiesa. *XVII ANIDIS Conference on "L'ingegneria sismica in Italia,"* 2017.
34. Cattari S, Degli Abbati S, Ottonelli D, Sivori D, Spacone E, Camata G, *et al. Task 4.1 Workgroup_Report di sintesi sulle attività svolte sugli edifici in muratura monitorati dall'Osservatorio Sismico delle Strutture, Linea Strutture in Muratura*. ReLUIS Report, Rete Dei Laboratori Universitari Di Ingegneria Sismica: 2017.
35. DPC. Osservatorio Sismico delle Strutture OSS Download Service. http://www.mot1.it/ossdownload.
36. Giresini L, Casapulla C, Denysiuk R, Matos J, Sassu M. Fragility curves for free and restrained

rocking masonry façades in one-sided motion. *Engineering Structures* 2018; **164**: 195–213. DOI: 10.1016/j.engstruct.2018.03.003.
37. Vasconcelos G, Lourenço PB. Experimental characterization of stone masonry in shear and compression. *Construction and Building Materials* 2009; **23**(11): 3337–3345.
38. Lourenço PB, Ramos LF. Characterization of cyclic behavior of dry masonry joints. *Journal of Structural Engineering* 2004; **130**(5): 779–786.
39. Lee HS, Park YJ, Cho TF, You KH. Influence of asperity degradation on the mechanical behavior of rough rock joints under cyclic shear loading. *International Journal of Rock Mechanics and Mining Sciences* 2001; **38**(7): 967–980. DOI: 10.1016/S1365-1609(01)00060-0.
40. Fajfar P. Capacity spectrum method based on inelastic demand spectra. *Earthquake Engineering & Structural Dynamics* 1999; **28**(9): 979–993. DOI: 10.1002/(SICI)1096-9845(199909)28:9<979::AID-EQE850>3.0.CO;2-1.
41. EC8-1. Eurocode 8: Design of structures for earthquake resistance—Part 1: General rules, seismic actions and rules for buildings 2004.
42. Ferrero C, Lourenço PB, Calderini C. 2016-2017 Central Italy Earthquake: Seismic Assessment of "Pietro Capuzi" School in Visso (Marche). *The 9th International Conference on Computational Methods (ICCM2018)*, 2018.